Supplementary Information

Implementation of slow magnetic relaxation in a SIM-MOF through a structural rearrangement

Javier Castells-Gil,[a] José J. Baldoví,[b] Carlos Martí-Gastaldo,[a] Guillermo Mínguez Espallargas*[a]

[a] Instituto de Ciencia Molecular, Universitat de València, Catedrático José Beltrán 2, E-46980 Paterna, Spain.

[b] Max Planck Institute for the Structure and Dynamics of Matter, Luruper Chaussee 149, D-22761 Hamburg, Germany.

E-mail: Guillermo.minguez@uv.es

Table of contents:

SI1. General considerations: starting materials and characterization

Materials and reagents

5-nitroisophthalic acid (98%), Dy(III) acetate hexahydrate (99.9 %), Gd(III) acetate hexahydrate, sodium hydroxide (98 %), acetic acid (99.7%) were purchased from Sigma-Aldrich, and used as received. *N,N*-Dimethylformamide (≥ 99.8%) were purchased from Scharlab. Ultrapure water from Milli-Q equipment was used when required. All reagents and solvents were used without any previous purification unless specified.

Physical and chemical characterization

- Carbon, nitrogen and hydrogen contents were determined by microanalytical procedures using a LECO CHNS.
- Thermogravimetric analysis were carried out with a Mettler Toledo TGA/SDTA 851 apparatus between 25 and 800 °C under ambient conditions (10 °C·min^{-1} scan rate and an air flow of 30 mL·min^{-1})
- NMR. ^{1}H spectra were run on a Bruker DRX300 spectrometer.
- XRD powder patterns were collected in a PANalytical X'Pert PRO diffractometer using copper radiation (Cu Kα = 1.5418 Å) with an X'Celerator detector, operating at 40 mA and 45 kV. Profiles were collected in the 2° < 2θ < 40° range with a step size of 0.013°.
- Optical microscope

SI2. Synthesis of materials

Synthesis of 3,3',5,5'-azobenzenetetracarboxylic acid (H4abtc): H4abtc was synthesized according to a reported method.[1] In a typical procedure, 5-nitroisophtalic acid (19 g) and sodium hydroxide (50 g) were suspended in 250 mL of Milli-Q water and reacted at 60 °C with continuous stirring for 1 hour. Next, glucose (100 g) was dissolved in 100 mL of warm water and the resulting solution was added dropwise to the yellow slurry that became dark brown due to reduction of the nitro groups. The mixture was left to cool down for 30 minutes followed by exposure to an air stream for 16 hours with continuous stirring at room temperature. Next, the crude was cooled in an ice bath prior to isolation of the solid by filtration with vacuum. Finally, the solid was dissolved in 250 mL of water and acidified with HCl 37% to produce an orange precipitate. This was isolated by filtration, thoroughly washed with water and dried in an oven (92% yield). Elemental analysis for C16H10N2O8: Calc. C (53.64), H (2.81), N (7.86); found: C (52.59), H (3.02), N (7.75). Spectroscopic data matched those quoted in the bibliography.[2]

Synthesis of MUV-4a: 0.3 mmol of $Dy(OAc)_3 \cdot 6H_2O$ (123.6 mg) and 0.225 mmol of H_4abtc (80.7 mg) were suspended in 12 mL of H_2O in a 25 mL Schott bottle. To this suspension, 63 mmol of acetic acid (3.6 mL) was added. The mixture was then sonicated for a few seconds, placed in an oven and heated at 160 ºC for 12 hours ($\uparrow$ +2.0 ºC min^{-1}, $\downarrow$ -0.4 ºC min^{-1}). Orange single crystals of **MUV-4a** were collected by filtration, washed thoroughly with DMF and water and dried under vacuum at room temperature overnight. Yield: 79.8% (based on H_4abtc).

Synthesis of Dy-MUV-4b: ca. 100 mg of **MUV-4a** were heated under vacuum at 150 ºC for 2h yielding a mixture of **MUV-4b** and MUV-4c, whose structures were solved by single crystal X-ray diffraction. However, the poor quality of the data corresponding to **MUV-4c** was not good enough for fully anisotropic refinement and therefore has not been deposited in the CCDC. Inmersion in water of this mixture comprised by **MUV-4b** and **MUV-4c** during 2 days yield the new phase **MUV-4d**, which was characterized as a single phase by XRPD. Further heating to 150 ºC under vacuum for 2h yields phase pure **MUV-4b**.

Synthesis of Gd-MUV-4a: Gd-MUV-4a was synthesized by following the same procedure described above but using $Gd(OAc)_3 \cdot 6H_2O$.
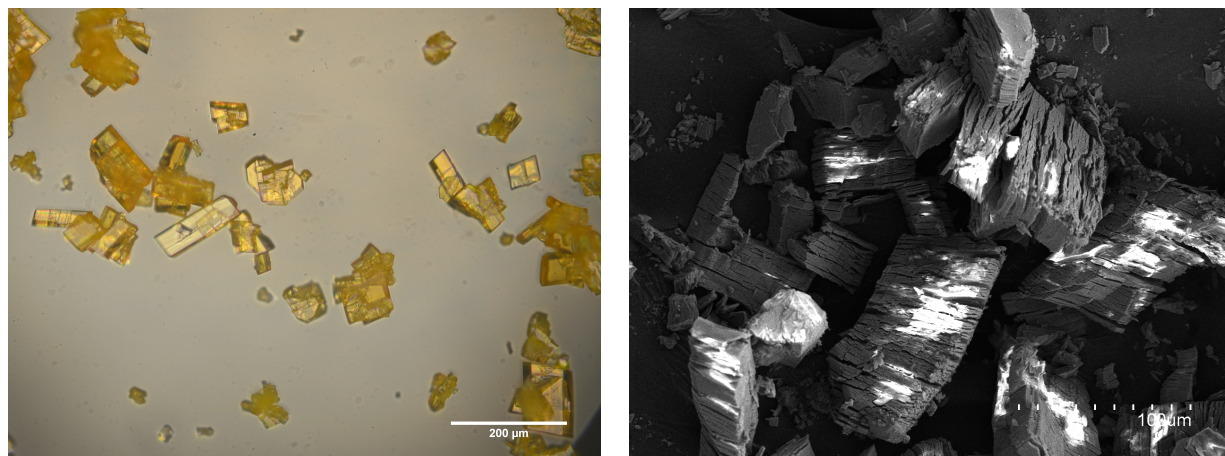
Figure S1 – Single-Crystals of MUV-4a observed with an optical microscope (left) and by SEM (right).

SI3. Crystallographic Data and Structure Refinemente of Dy-MUV-4a

X-Ray diffraction

A suitable crystal was selected, mounted on a Mitagen micromont by using paraffin oil and measured on a Super-Nova, Single source at offset, Sapphire3 diffractometer. The crystal was kept at 120.00(10) K during data collection. The structure was solved in Olex2[3] by using the ShelXT structure solution program using Intrinsic Phasing and refined with the ShelXL refinement package using Least Squares minimisation.

Table S1. Crystal data and structure refinement for **MUV-4a** and **MUV-4b.**

	MUV-4a	MUV-4b
Identification code	CCDC 1855292	CCDC 1855294
Empirical formula	C16H14.2DyN2O11.7	C16H10.52DyN2O9.76
Formula weight	584.48	549.44
Temperature/K	120.00(10)	120(2)
Crystal system	triclinic	triclinic
Space group	P-1	P-1
a/Å	6.6676(3)	7.1771(2)
b/Å	10.1303(5)	9.0830(3)
c/Å	13.8039(6)	13.2629(4)
α/°	74.983(4)	109.487(3)
β/°	78.546(4)	90.285(2)
γ/°	83.143(4)	92.121(3)
Volume/Å3	880.33(7)	814.38(5)
Z	2	2
ρcalcg/cm3	2.205	2.241
μ/mm-1	4.319	4.653
F(000)	568.0	529.0
Crystal size/mm3	0.157 × 0.122 × 0.055	0.044 × 0.035 × 0.021
Radiation	MoKα (λ = 0.71073)	MoKα (λ = 0.71073)
2Θ range for data collection/°	5.772 to 49.422	5.682 to 49.426
Index ranges	-7 ≤ h ≤ 7, -11 ≤ k ≤ 11, -16 ≤ l ≤ 16	-8 ≤ h ≤ 8, -10 ≤ k ≤ 10, -15 ≤ l ≤ 15
Reflections collected	9519	11040
Independent reflections	2996 [Rint = 0.0529, Rsigma = 0.0546]	2785 [Rint = 0.0773, Rsigma = 0.0699]
Data/restraints/parameters	2996/17/304	2785/0/276
Goodness-of-fit on F2	1.071	1.039
Final R indexes [I>=2σ (I)]	R1 = 0.0262, wR2 = 0.0557	R1 = 0.0385, wR2 = 0.0766
Final R indexes [all data]	R1 = 0.0290, wR2 = 0.0573	R1 = 0.0478, wR2 = 0.0806
Largest diff. peak/hole / e Å-3	0.71/-0.84	1.22/-1.03

MUV-4a: Refinement model description: number of restraints – 17; number of constraints – 0.

MUV-4b: Refinement model description: number of restraints – 0; number of constraints – 0.
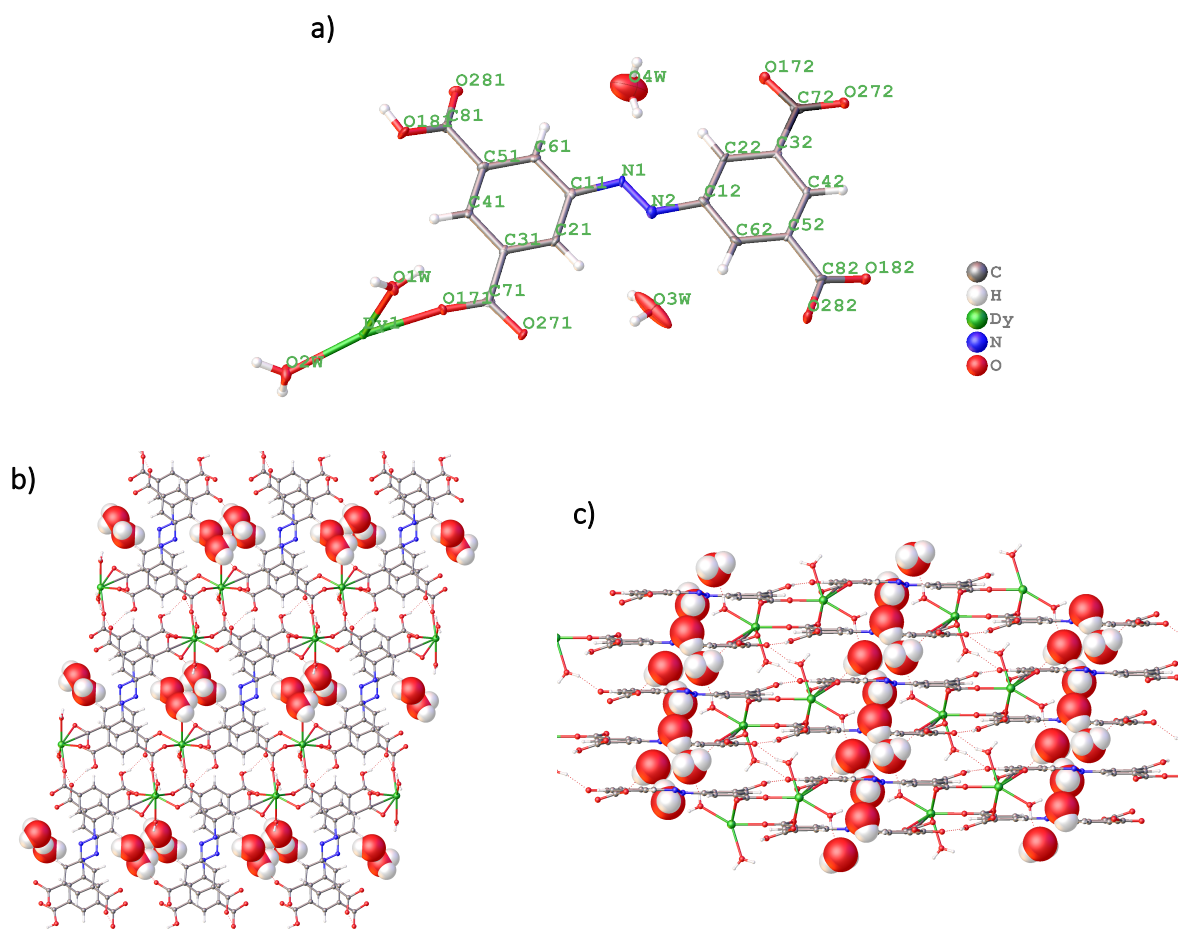
Figure S2. Structure of **MUV-4a**. a) ORTEP representation (50 % probability) of the assymetric unit of **MUV-4a** and view of the structure along b) the a-axis and c) the b-axis.
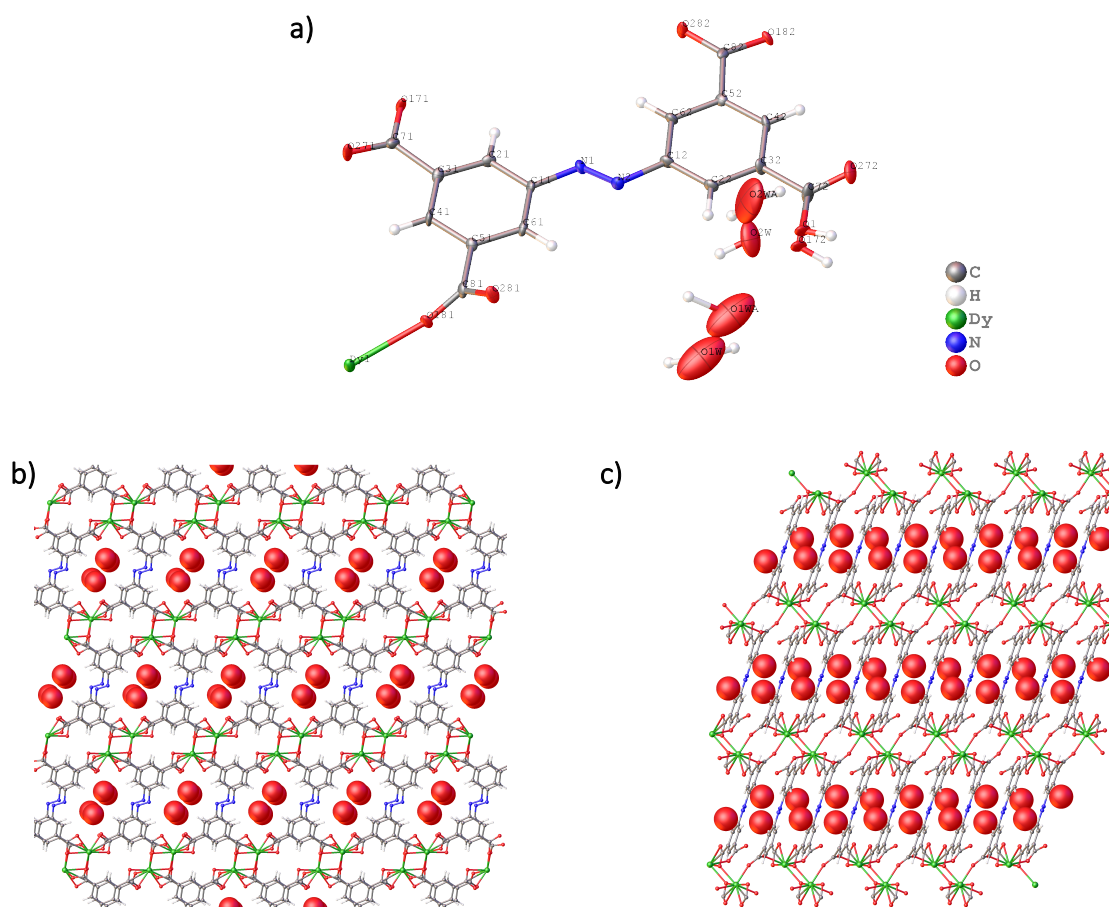
Figure S3. Structure of **MUV-4b**. a) ORTEP representation (50 % probability) of the assymetric unit of **MUV-4b** and view of the structure along b) the a-axis and c) the b-axis.
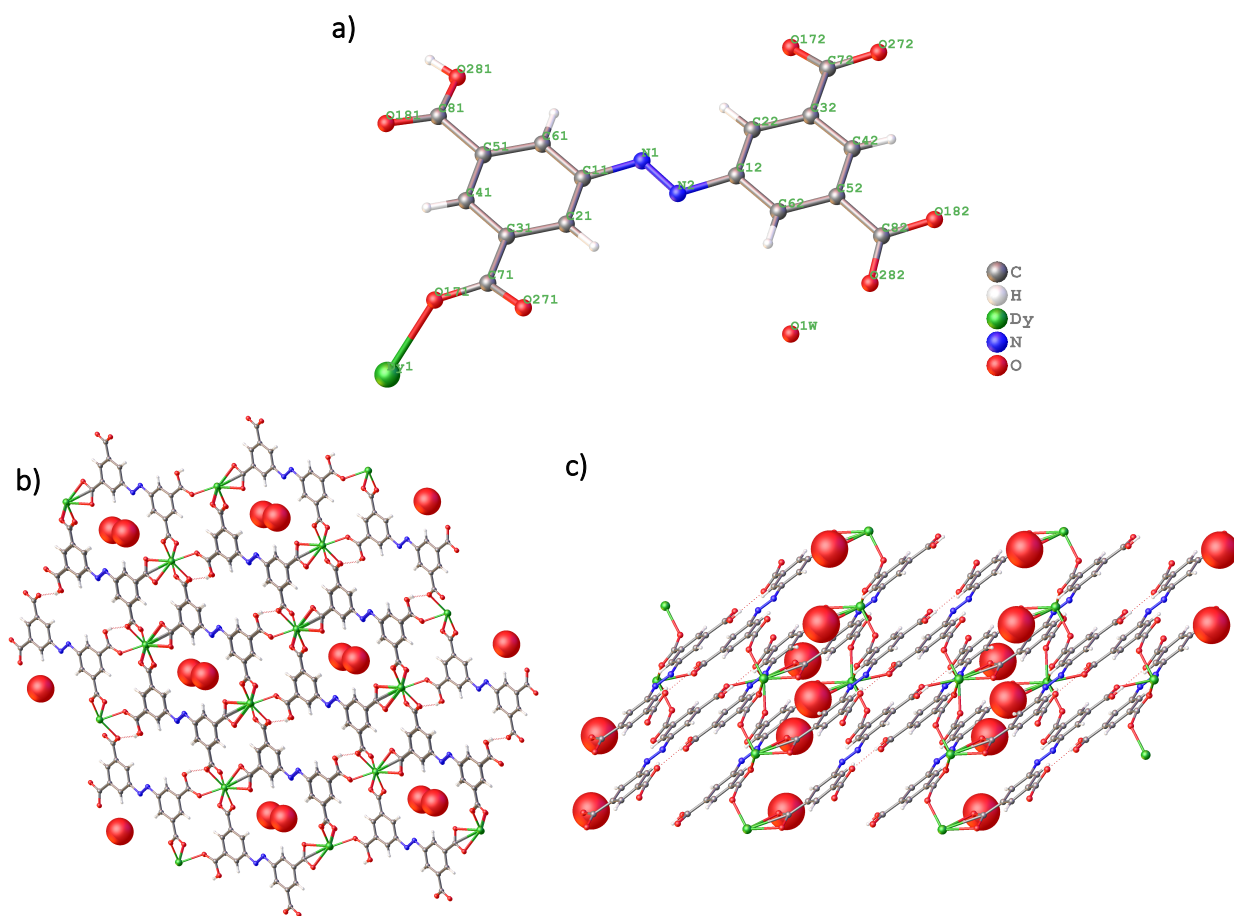
Figure S4. Structure of **MUV-4c**. a) representation of the assymetric unit of **MUV-4c** and view of the structure along b) the a-axis and c) the b-axis.

Table S2. Shortest and longest Dy-Dy distances in **MUV-4a-c**

	Shortest d_{Dy-Dy} (Å)	Longest d_{Dy-Dy} (Å)
MUV-4a	5.462	6.294
MUV-4b	4.051	5.768
MUV-4c	4.737	-
MUV-4d	N/A	N/A

Powder X-Ray Diffraction (PXRD)

Powder XRD patterns were collected for polycrystalline samples using a 0.5 mm glass capillary mounted and aligned in a PANalytical Empyrean diffractometer (Bragg-Brentano geometry) using copper radiation (Cu Kα λ= 1.5418 Å) with an PIXcel detector, operating at 40 mA and 45 kV. Profiles were collected by using a Soller Slit of 0.04° and a divergence slit of ½ at room temperature in the angular range 2° < 2θ < 40° with a step size of 0.013°.
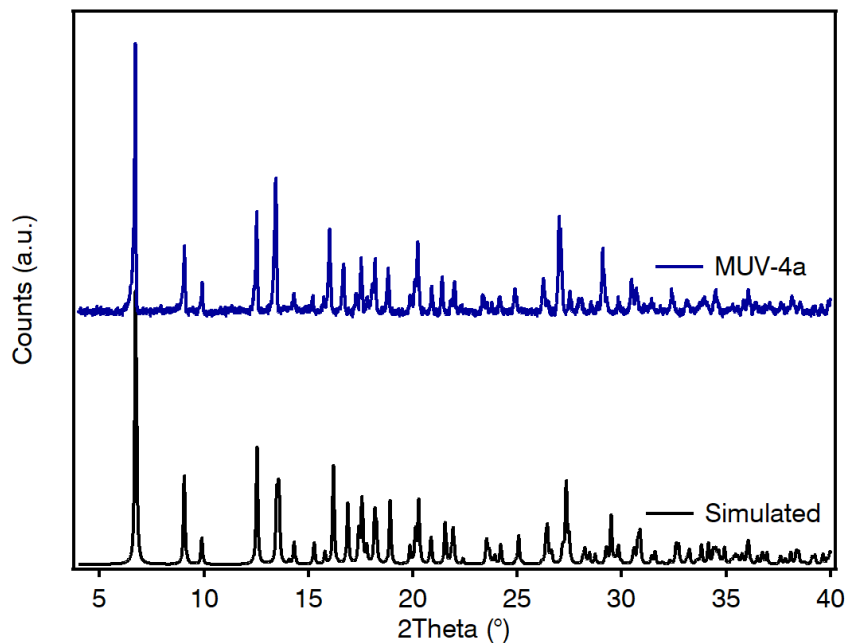
Figure S5. Experimental (blue) and simulated (black) powder X-Ray diffractogram of **MUV-4a**.
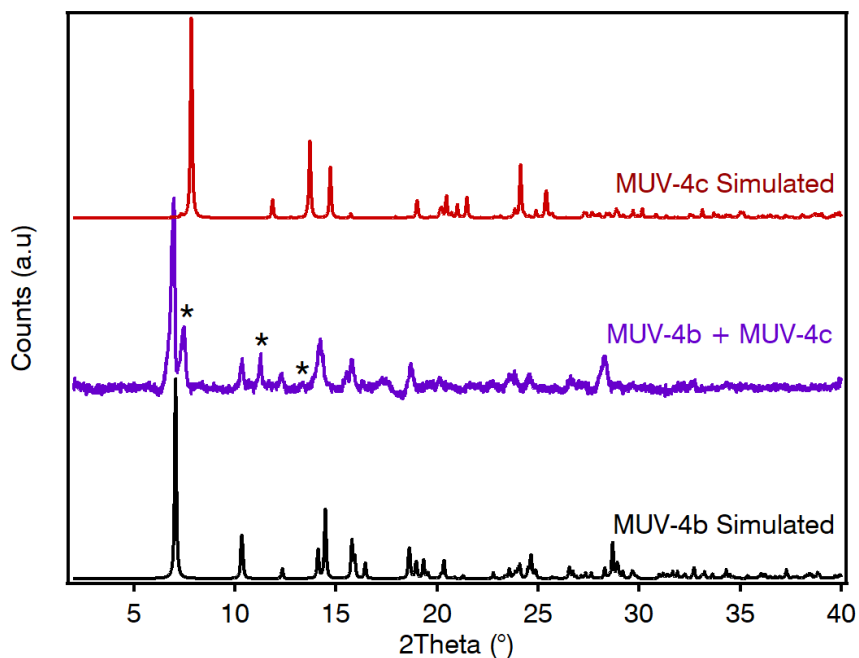
Figure S6. Experimental (orange) powder X-Ray diffractogram of **MUV-4b-c** compared to the simulated diffractograms of **MUV-4b** (black) and **MUV-4c** (red). The peaks marked with * refer to the observed peaks of MUV-4c phase.
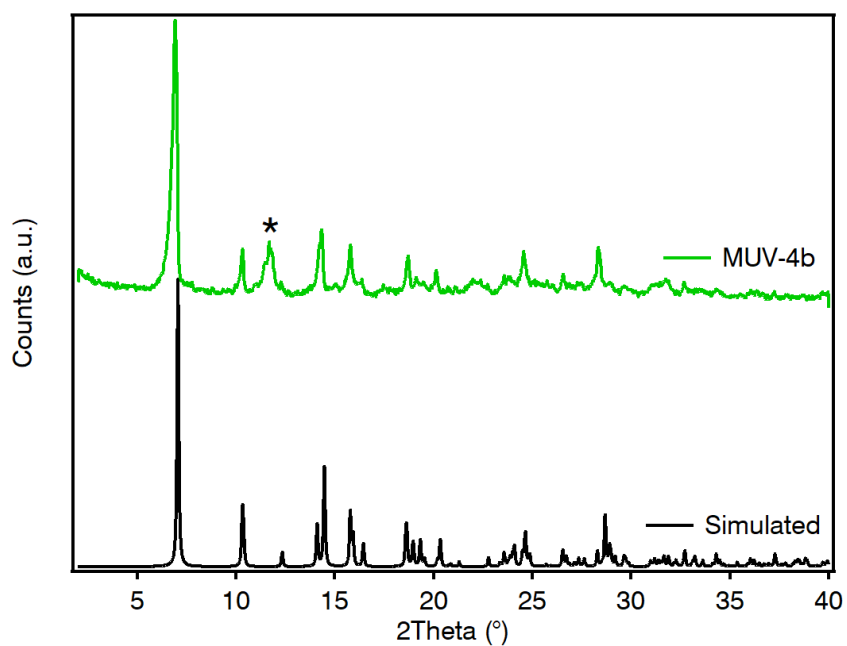
Figure S7. Experimental (green) and simulated (black) powder X-Ray diffractogram of **MUV-4b.** A small peak (*) not predicted by the simulation that we could not identify is observed in all cases.
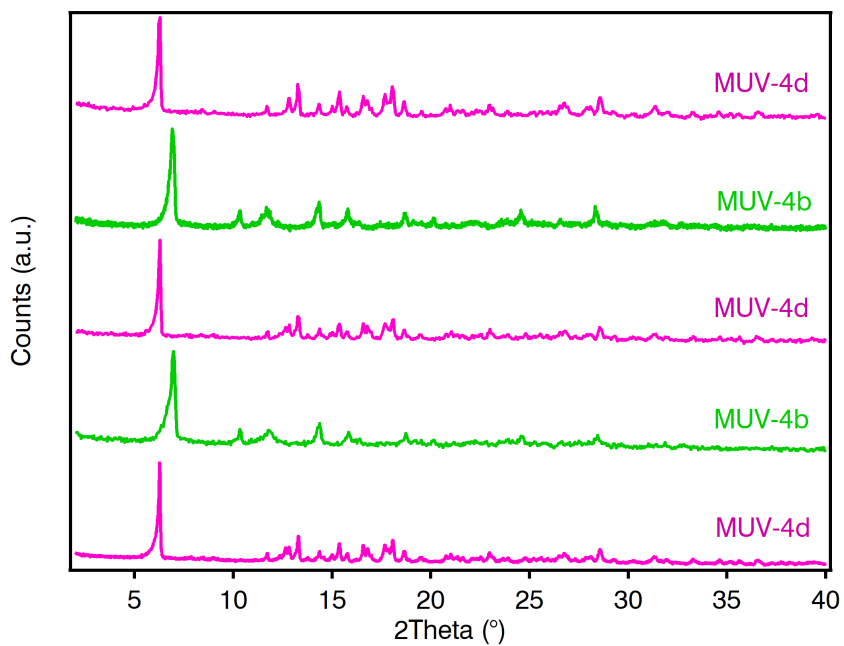
Figure S8. Powder X-Ray diffractogram of **MUV-4d** after desolvation and subsequent rehydration.
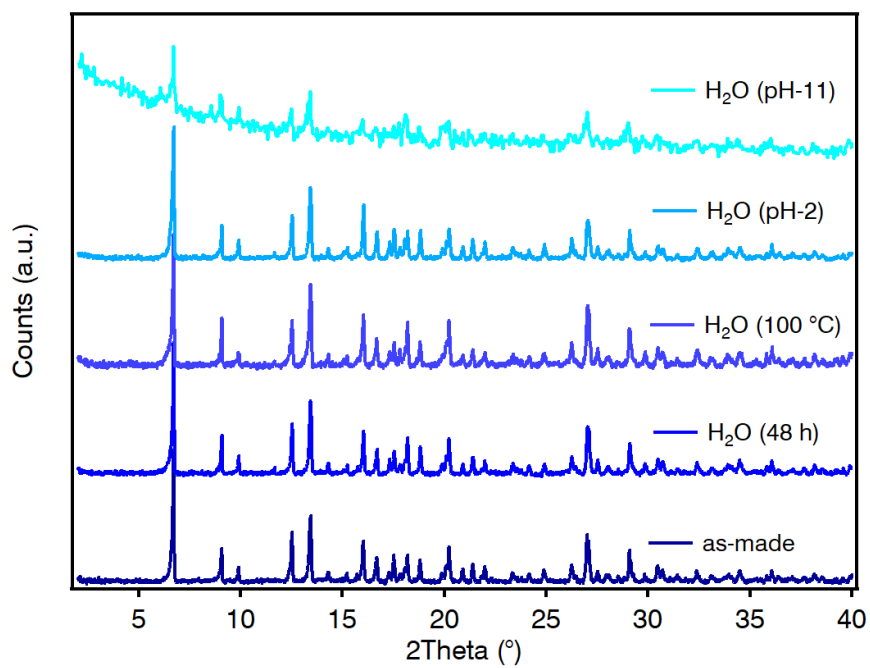
Figure S9. Powder X-Ray diffractograms of **MUV-4a** soaked in H_2O under different conditions.
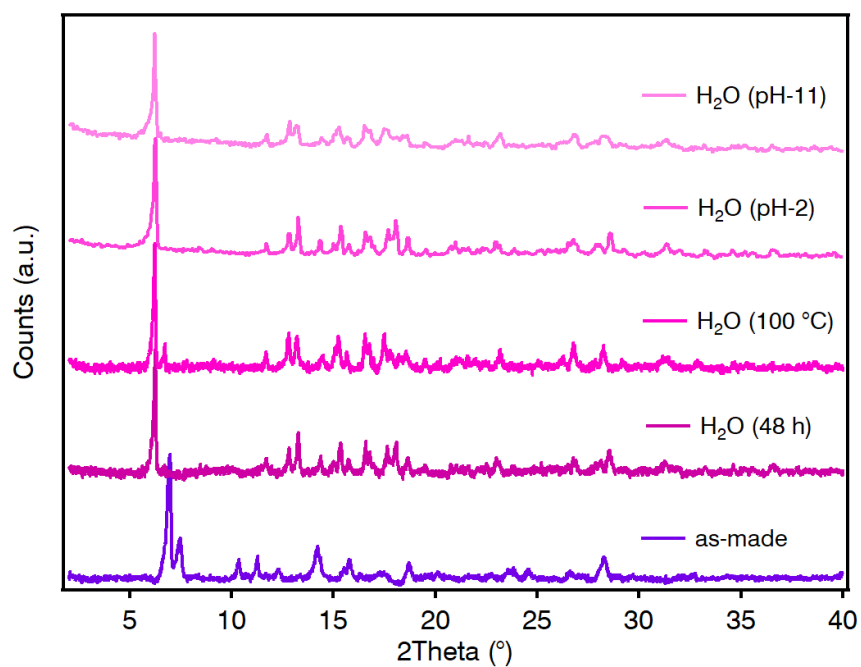
Figure S10. Powder X-Ray diffractograms of **MUV-4b** soaked in H_2O under different conditions.

Thermogravimetric analysis

MUV-4a (Figure S7) is thermally stable up to 400 °C. It shows a first weight loss of 11.22 % close to 100 °C, that corresponds to the loss of 3.7 molecules of water (Calc: 11.39 %), i.e 2 water molecules in the pores (one of them with a partial occupancy of 70 %, as determined from crystallographic data) plus the 2 water molecules coordinated to the Dy^{III} ion. This is followed by a plateau up to 400 °C where the decomposition of the framework takes place to form Dy_2O_3. **MUV-4b** and **MUV-4d** (Figure S8-9) show a similar thermal stability to **MUV-4a**. In case of **MUV-4d**, the first weight loss of 16.63 % observed corresponds to approximately 5.7 molecules of water (Calc: 16.58 %).
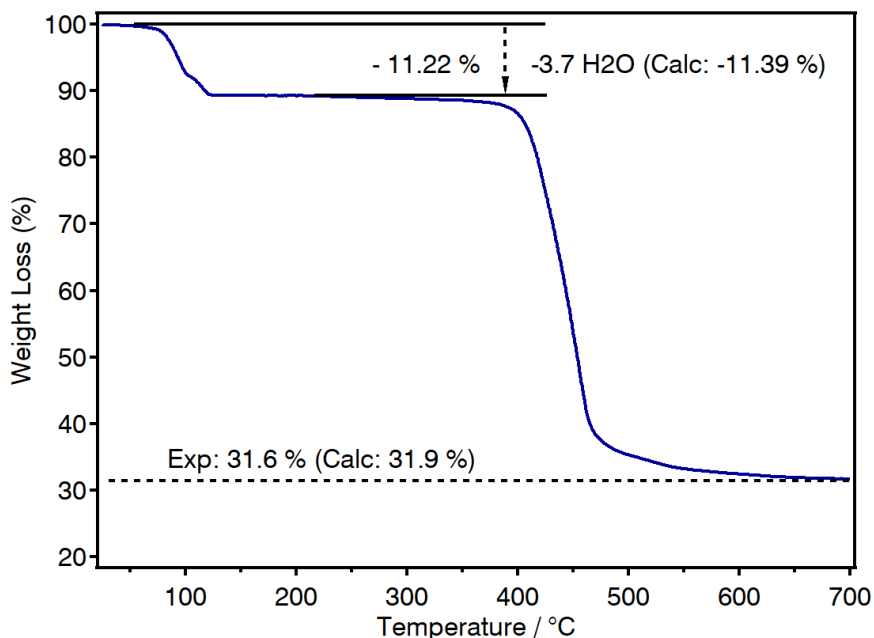
Figure S11. TGA of **MUV-4a** in air between 25 and 700 °C
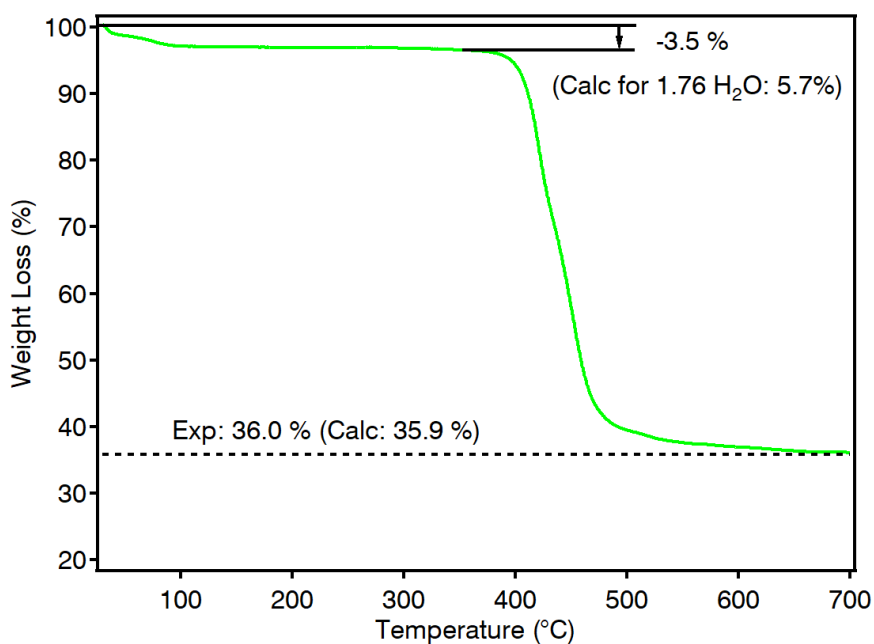
Figure S12. TGA of **MUV-4b** in air between 25 and 700 °C
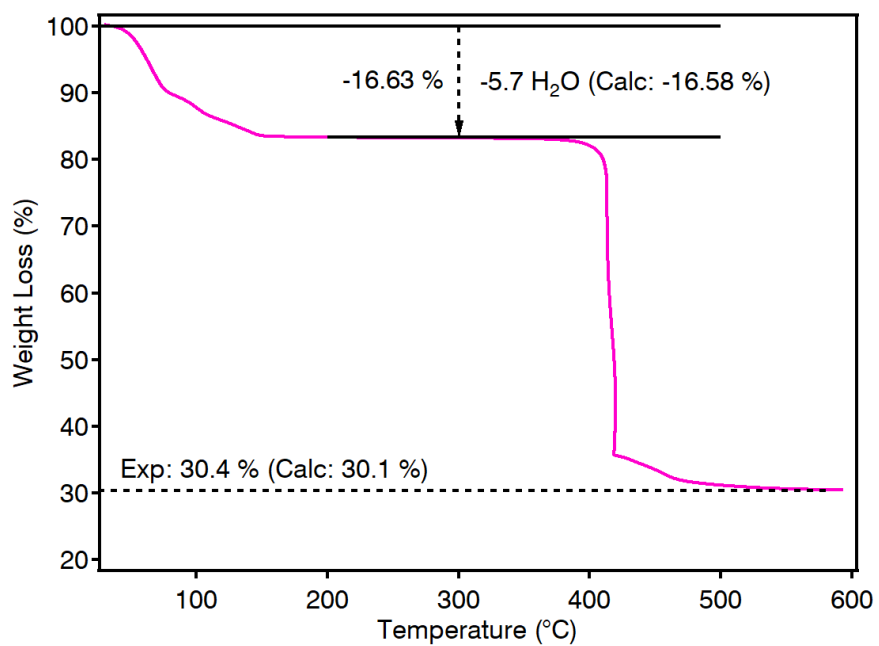
Figure S13. TGA of **MUV-4d** in air between 25 and 600 °C

Magnetic Measurements

Magnetic measurements Magnetic measurements were performed with a Quantum Design Physical Property Measurement System (PPMS). Variable-temperature (2.0–300 K) direct current (dc) magnetic susceptibility measurements were carried out in an applied field of 1.0 kG and variable field magnetisation measurements up to 5 T at 2.0 K. Variable-temperature (2.010 K) alternating current (ac) magnetic susceptibility measurements in a ±4.0 G oscillating field at frequencies in the range of 1.0– 1000.0 Hz were carried out in a zero dc field and in a dc field of 1.0 kG.
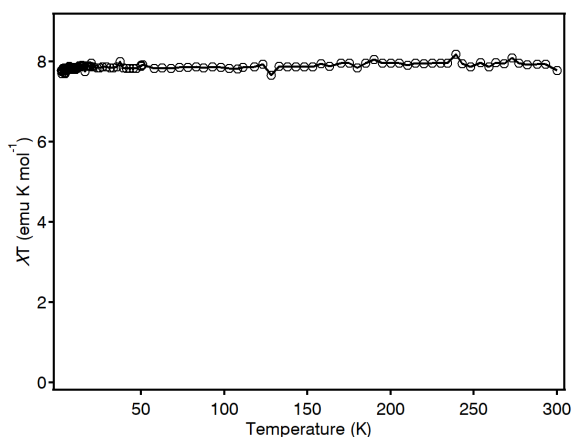
Figure S14. Variation of the product χT with the temperature for **Gd-MUV-4a**
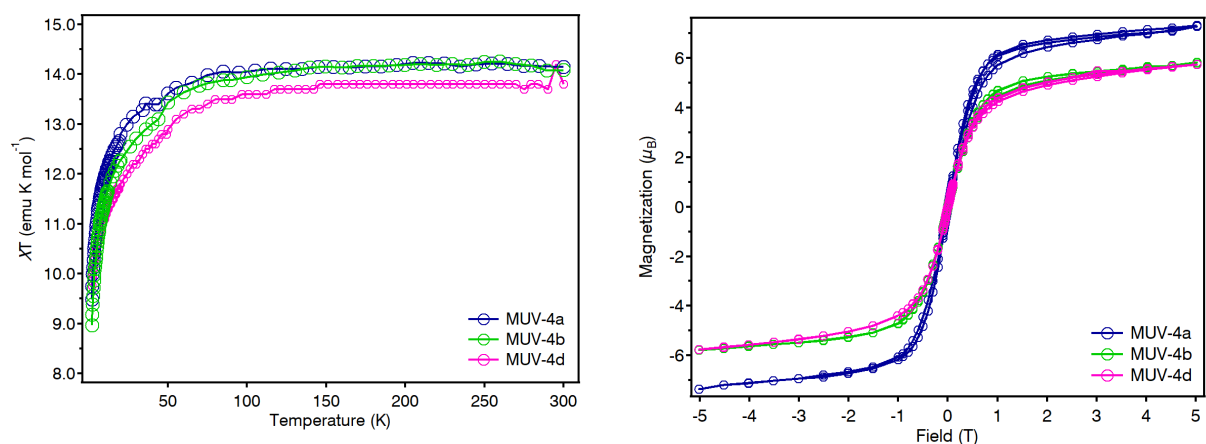
Figure S15. DC magnetic measurements of **MUV-4a**, **MUV-4b** and **MUV-4d.** Variation of the product χT with the temperature (left) and magnetic hysteresis loops collected at 2K.
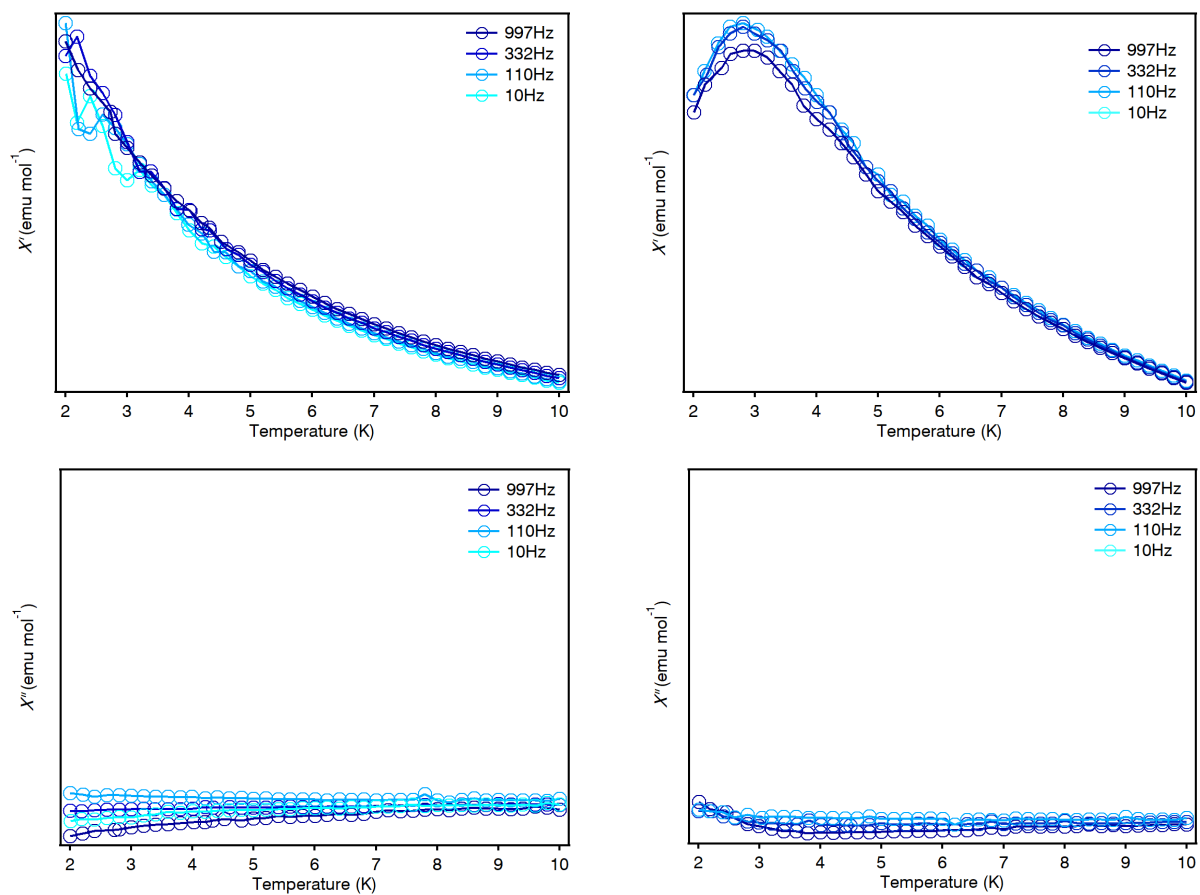
Figure S16. In-phase (top) and out-of-phase (bottom) dynamic magnetic susceptibility of **MUV-4a** under an external magnetic field of 0 G (left) and 1000 G (right).
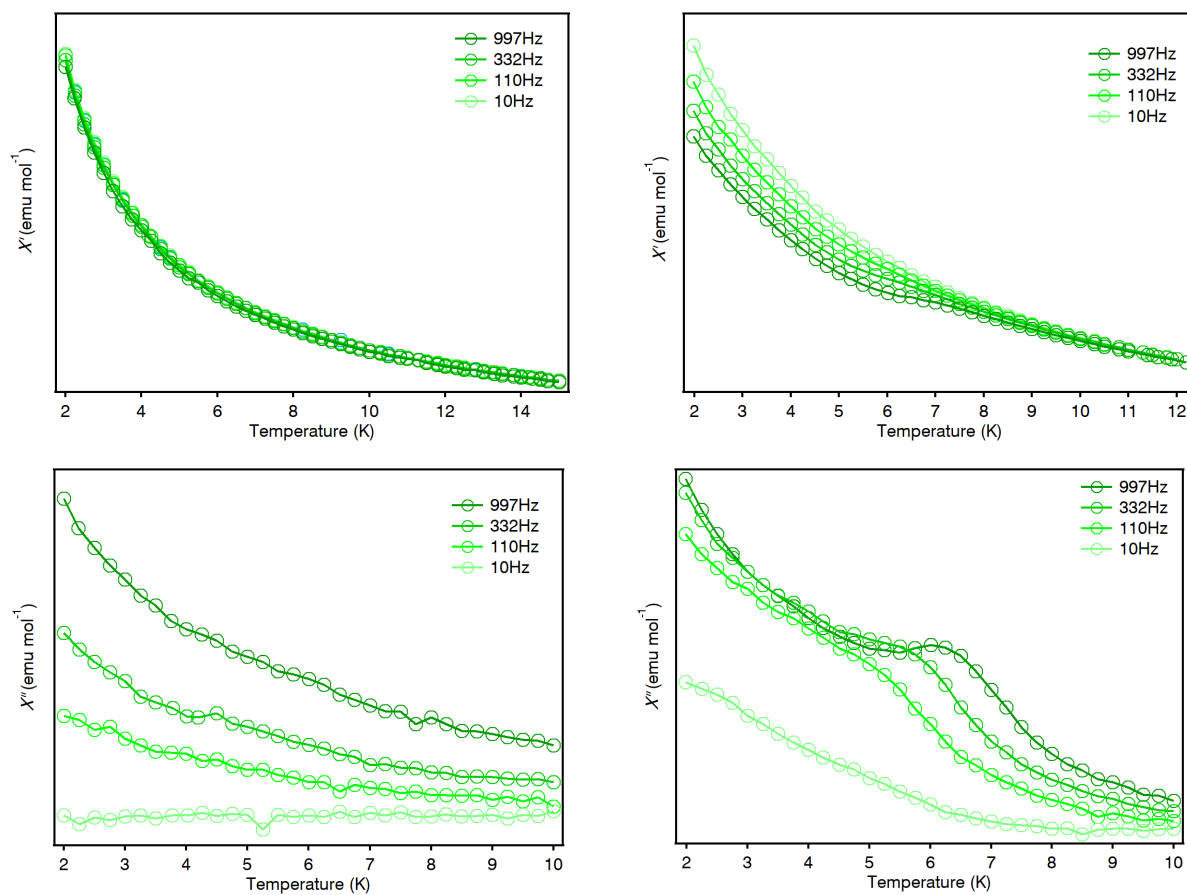
Figure S17. In-phase (top) and out-of-phase (bottom) dynamic magnetic susceptibility of **MUV-4b** under an external magnetic field of 0 G (left) and 1000 G (right).
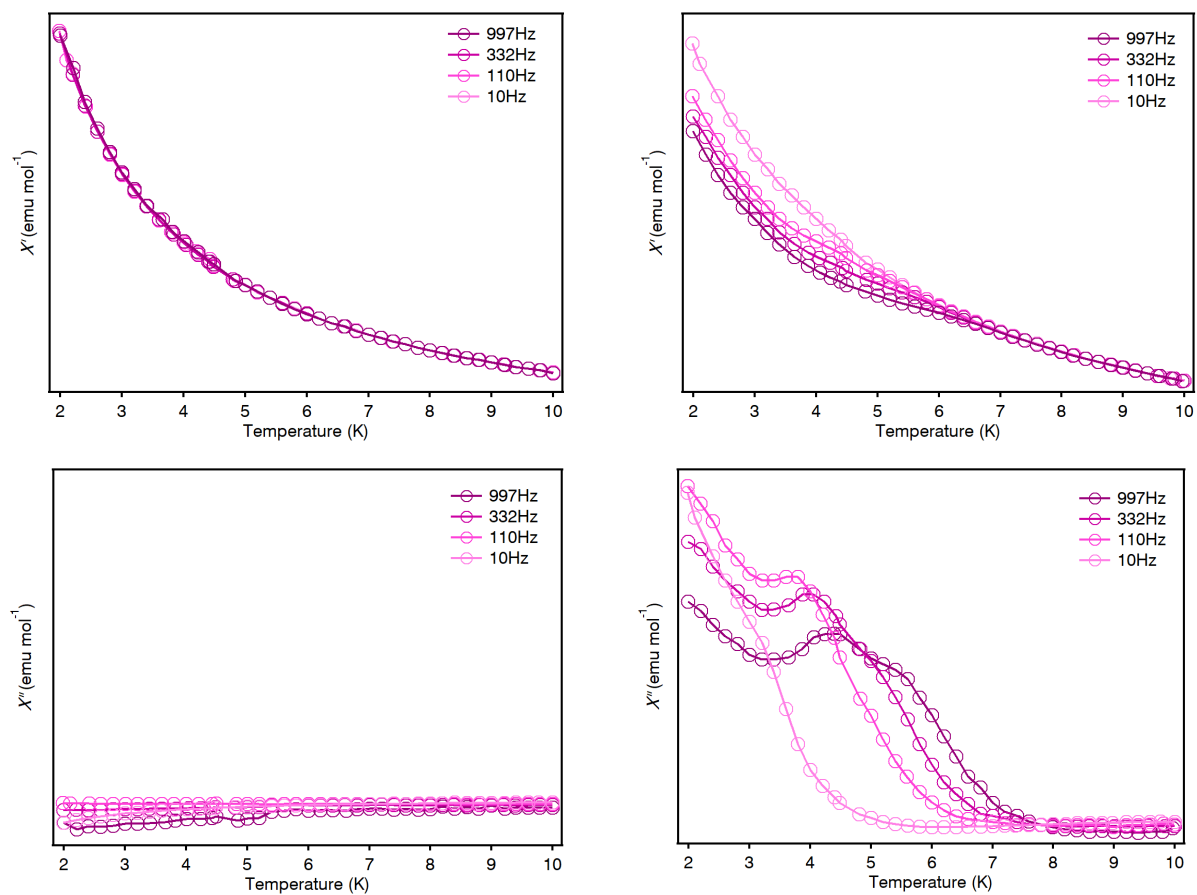
Figure S18. In-phase (top) and out-of-phase (bottom) dynamic magnetic susceptibility of **MUV-4d** under an external magnetic field of 0 G (left) and 1000 G (right).

SI4. Theoretical calculations

The model that we have applied in order to understand the different static magnetic properties of **MUV-4a** and **MUV-4b** is the Radial Effective Charge (REC) model. Such a model is an electrostatic *semi-empirical* crystal field approach commonly used in molecular magnetism, which povides an estimation of the crystal field parameters (CFPs) and permit to rationalize the magnetic properties of a particular *f*-block coordination complex.[3] From the calculated CFPs, the model estimates the ground-*J* multiplet energy levels and their corresponding wave functions, composed by the different M_J microstates. This kind of calculations use the crystallographic atomic coordinates of the first coordination sphere around the magnetic centre as an input. The software code that has this model implemented is the SIMPRE computational package,[4] which parameterizes the electric field effect produced by the surrounding ligands by using the following Crystal Field Hamiltonian expressed in terms of the Extended Stevens Operators (ESOs)[5]:

$$\hat{H}_{cf}(J) = \sum_{k=2,4,6} \sum_{q=-k}^{k} B_k^q O_k^q = \sum_{k=2,4,6} \sum_{q=-k}^{k} a_k (1-\sigma_k) A_k^q \left\langle r^k \right\rangle O_k^q \tag{1}$$

where *k* is the order (also called rank or degree) and *q* is the operator range, that varies between *k* and −*k*, of the Stevens operator equivalents O_k^q as defined by Ryabov in terms of the angular momentum operators $J_\pm$ and J_z,[6] where the components $O_k^q(c)$ and $O_k^q(s)$ correspond to the ESOs with q ≥ 0 and q < 0 respectively.[6] Note that all the Stevens CF parameters B_k^q are real, whereas the matrix elements of O_k^q (q < O) are imaginary. a_k are the α, β and γ Stevens coefficients[7] for *k* = 2, 4, 6, respectively, which are tabulated and depend on the number of *f* electrons. σ_k are the Sternheimer shielding parameters[8] of the 4*f* electronic shell, and <r^k> are the expectation values of the radius.[8]

In the code, the A_k^q CF parameters are calculated through the following expressions:

$$A_k^0 = \frac{4\pi}{2k+1} \sum_{i=1}^{N} \frac{Z_i e^2}{R_i^{k+1}} Z_{k0}(\theta_i, \varphi_i) p_{kq} \tag{2.a}$$

$$A_k^q = \frac{4\pi}{2k+1} \sum_{i=1}^{N} \frac{Z_i e^2}{R_i^{k+1}} Z_{kq}^c(\theta_i, \varphi_i) p_{kq} \tag{2.b}$$

$$A_k^q = \frac{4\pi}{2k+1} \sum_{i=1}^{N} \frac{Z_i e^2}{R_i^{k+1}} Z_{k|q|}^s(\theta_i, \varphi_i) p_{k|q|} \tag{2.c}$$

and the effect of the ligand is modeled through an effective point charge situated between the lanthanoid and the coordinated atom at a distance R_i from the magnetic centre, which is smaller than the real metal-ligand distance (r_i). To account for the effect of covalent electron sharing, a radial displacement vector (D_r) is defined, in which the polar coordinate *r* of each coordinated atom is varied, $R_i = r_i$-D_r. The usual procedure is to obtain the D_r parameter of each kind of donor atom fitting an observable (e.g. energy levels or magnetic properties). At the same time, the charge value (Z_i) is scanned in order to achieve the minimum deviation between calculated and experimental data, whereas θ_i and φ_i remain constant. This allows to inexpensively correlate the chemical structure with crystal field effects. In the fitting procedure, we define the relative error *E* as:

$$E = \frac{1}{n} \sum_{i=1}^{n} \frac{\left[\chi_{theo,i} T_i - \chi_{\exp,i} T_i \right]^2}{\left[\chi_{\exp,i} T_i \right]^2} \tag{3}$$

where $\chi_{exp}T$ and $\chi_{theo}T$ are experimental and theoretical values, respectively, and n is the number of points.

In this work, we have distinguished between two different types of oxygen atoms: (1) O that belong to the carboxylate ligands, and (2) O of the water molecules. Thus, we have started our fit of the magnetic properties using the MUV-4b experimental data, obtaining D_r = 0.885 Å and Z_i = 0.1024 for the carboxylate oxygen atoms, achievening an excellent reproduction of the χT product (relative error of E = 5.825·10^{-5}). With these parameters, we predicted the magnetization vs magnetic field curve at 2K, which resulted to be in good agreement with the experimental data. Then, we have extrapolated these parameters to the carboxylate oxygen atoms of MUV-4a, varying only the two REC parameters of the water oxygens in order to fit the experimental data. The effect of the water oxygens could be modeled with D_r = 0.850 Å and Z_i = 0.125, with E = 1.009·10^{-4}. Here it is worth to mention that these phenomenological parameters used by SIMPRE to predict the spin-energy levels and wave functions do not pretend to simulate an actual charge distribution. The resulting set of CFPs, energy levels and compositions of the wave functions are reported in Tables S2 and S3.

Table S3. Crystal-field parameters ($A_k^q < r^k >$; Stevens notation) in cm^{-1} obtained for **MUV-4a** and **MUV-4b**.

k	q	MUV-4a	MUV-4b
2	0	33.61	57.09
2	1	-185.21	-172.78
2	-1	199.00	12.79
2	2	197.36	19.13
2	-2	40.90	83.21
4	0	64.40	31.95
4	1	50.15	145.85
4	-1	-130.19	-148.69
4	2	-97.13	234.18
4	-2	-16.67	-163.55
4	3	720.97	690.63
4	-3	-423.07	23.39
4	4	-31.16	49.32
4	-4	-270.92	265.79
6	0	-1.71	-5.43
6	1	-35.85	129.73
6	-1	-14.79	-74.66
6	2	76.43	42.79
6	-2	58.10	21.41
6	3	30.96	-175.84
6	-3	-27.23	1.07
6	4	-0.90	11.59
6	-4	83.09	-39.14
6	5	358.92	237.86
6	-5	78.75	-115.59
6	6	80.01	-94.74
6	-6	-172.49	-76.97

Table S4. Ground multiplet energy level scheme (Kramers doublets in cm^{-1}) and main |M$_J$> contributions to the wave function calculated for **MUV-4a** and **MUV-4b.**

MUV-4a		MUV-4b	
0	76.2% |±15/2> + 6.6% |±1/2>	**0**	76.3% |±15/2> + 8.7% |±11/2> + 7.7% |±9/2>
12	29.5% |±1/2> + 20.6% |∓3/2> + 15.8% |±15/2> + 11.0% |∓1/2> + 8.5% |±5/2> + 6.8% |±3/2>	**30**	20.0% |±7/2> + 17.9% |±13/2> + 15.6% |∓1/2> + 14.2% |±5/2> + 9.5% |∓3/2> + 5.7% |∓5/2>
46	28.6% |±5/2> + 14.2% |±7/2> + 14.2% |±3/2> + 9.9% |∓3/2> + 6.7% |∓7/2> + 6.2% |∓5/2> + 5.9% |±9/2>	**48**	23.7% |±3/2> + 16.7% |±5/2> + 14.1% |±1/2> + 10.4% |±15/2> + 6.2% |∓9/2>
79	23.6% |±13/2> + 12.5% |±1/2> + 12.1% |±7/2> + 10.5% |∓3/2> + 9.0% |∓5/2> + 7.8% |±3/2> + 7.8% |∓1/2> + 7.5% |±9/2>	**54**	29.3% |±13/2> + 14.4% |∓3/2> + 8.4% |∓7/2> + 8.1% |∓5/2> + 7.1% |∓9/2> + 6.8% |±9/2> + 6.3% |±7/2> + 5.1% |±1/2>
97	35.5% |±13/2> + 16.0% |±9/2> + 14.3% |±11/2> + 5.7% |±7/2> + 5.4% |∓7/2>	**89**	24.0% |±11/2> + 17.3% |±13/2> + 9.2% |±1/2> + 7.5% |±9/2> + 7.1% |±5/2> + 5.9% |∓1/2> + 5.4% |±7/2> + 5.3% |∓5/2> + 5.3% |∓9/2>
110	20.6% |±11/2> + 13.9% |±9/2> + 11.7% |±7/2> + 11.5% |∓13/2> + 10.1% |±5/2> + 7.9% |∓5/2> + 5.7% |±1/2>	**144**	24.5% |±11/2> + 21.4% |±9/2> + 13.1% |±7/2> + 9.4% |±1/2> + 6.8% |±13/2> + 6.4% |±3/2> + 6.1% |∓1/2>
149	37.5% |±11/2> + 24.6% |±9/2> + 14.6% |±13/2> + 13.8% |±7/2>	**188**	24.6% |±9/2> + 23.9% |±11/2> + 22.2% |±13/2> + 12.7% |±7/2> + 6.4% |±15/2> + 5.1% |±5/2>
281	20.2% |±9/2> + 19.1% |±7/2> + 16.2% |±5/2> + 15.3% |±11/2> + 11.3% |±3/2> + 6.6% |±1/2>	**219**	24.7% |±5/2> + 21.3% |±3/2> + 16.3% |±7/2> + 13.9% |±1/2> + 7.8% |∓1/2> + 5.1% |±9/2>

Table S5. Ground multiplet energy level scheme (Kramers doublets in cm^{-1}) and main |M$_J$> contributions to the wave function calculated for **MUV-4a** considering all the donor atoms as carboxylates.

MUV-4a (all carboxylates)	
0	86.1% |±15/2>
18	5.9% |±15/2> + 11.6% |±5/2> + 11.6% |±3/2> + 32.0% |±1/2> + 14.2% |∓1/2> + 17.8% |∓3/2>
51	13.2% |±7/2> + 27.7% |±5/2> + 19.3% |±3/2> + 9.6% |∓3/2> + 6.6% |∓5/2> + 5.8% |∓7/2>
79	21.6% |±13/2> + 8.9% |±9/2> + 12.1% |±7/2> + 5.9% |±3/2> + 15.1% |±1/2> + 7.5% |∓1/2> + 7.8% |∓3/2> + 9.5% |∓5/2>
100	39.3% |±13/2> + 16.5% |±11/2> + 14.0% |±9/2> + 5.0% |±1/2>
118	17.7% |±11/2> + 7.1% |±9/2> + 19.0% |±7/2> + 15.9% |±5/2> + 6.8% |±3/2> + 7.8% |±1/2> + 7.0% |∓9/2> + 9.7% |∓13/2>
149	11.6% |±13/2> + 35.0% |±11/2> + 29.0% |±9/2> + 14.5% |±7/2>
284	5.6% |±13/2> + 16.7% |±11/2> + 20.3% |±9/2> + 18.7% |±7/2> + 15.5% |±5/2> + 10.5% |±3/2> + 6.0% |±1/2>
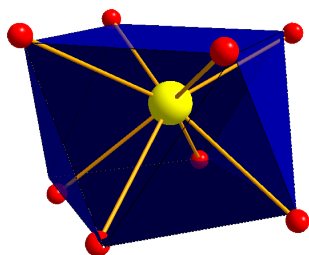
Square Antiprism

(D_{4d})
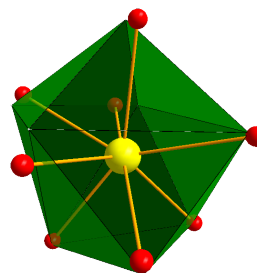
Triangular Dodecahedron

(D_{2d})

Figure S19. Square Antiprism (blue) and triangular dodecahedron (green) geometries encountered in MUV-4a and MUV-4b, respectively, as calculated by the software SHAPE.[9]

SI6. References.

1   P. S. Z. Sardar Ameerunisha, J. Chem. Soc. Perkin Trans. 2, 1995, 1679.

2   C. Qin, Y. Feng, H. An, J. Han, C. Cao and W. Feng, ACS Appl. Mater. Interfaces, 2017, 9, 4066–4073.

3   Baldoví, J. J.; Borrás-Almenar, J. J.; Clemente-Juan, J. M.; Coronado, E.; Gaita-Ariño, A. Dalton Trans. 2012, 41, 13705

4   Baldoví, J. J.; Cardona-Serra, S.; Clemente-Juan, J. M.; Coronado, E.; Gaita-Ariño, A.; Palii, A. J. Comput. Chem. 2013, 34, 1961–1967

5   C. Rudowicz, C.Y. Chung, J. Phys. Condens. Matter, 2004, 16, 5825; (b) C. Rudowicz, 1985, J. Phys. C: Solid State Phys., 18, 1415; (c) C. Rudowicz, 1985b, J. Phys. C: Solid State Phys., 18, 3837 (erratum)

6   I.D. Ryabov, Journal of Magnetic Resonance, 1999, 140, 141

7   K. W. H. Stevens, Proc.Phys. Soc. 1952, 65, 209

8   S. Edvardsson, M. Klinterberg, Journal of Alloys and Compounds, 1998, 275, 233

9   Llunell, M.; Casanova, D.; Girera, J.; Alemany, P.; Alvarez, S. SHAPE, version 2.0; Universitat de Barcelona: Barcelona, Spain, 2010.